Temporal manipulation of *Cdkl5* reveals essential postdevelopmental functions and reversible CDKL5 deficiency disorder–related deficits

Barbara Terzic,[1] M. Felicia Davatolhagh,[2] Yugong Ho,[1] Sheng Tang,[1] Yu-Ting Liu,[1] Zijie Xia,[1] Yue Cui,[1] Marc V. Fuccillo,[2] and Zhaolan Zhou[1]

[1]Department of Genetics and [2]Department of Neuroscience, Perelman School of Medicine, University of Pennsylvania, Philadelphia, Pennsylvania, USA.

CDKL5 deficiency disorder (CDD) is an early onset, neurodevelopmental syndrome associated with pathogenic variants in the X-linked gene encoding cyclin-dependent kinase-like 5 (CDKL5). CDKL5 has been implicated in neuronal synapse maturation, yet its postdevelopmental necessity and the reversibility of CDD-associated impairments remain unknown. We temporally manipulated endogenous *Cdkl5* expression in male mice and found that postdevelopmental loss of CDKL5 disrupts numerous behavioral domains, hippocampal circuit communication, and dendritic spine morphology, demonstrating an indispensable role for CDKL5 in the adult brain. Accordingly, restoration of *Cdkl5* after the early stages of brain development using a conditional rescue mouse model ameliorated CDD-related behavioral impairments and aberrant NMDA receptor signaling. These findings highlight the requirement of CDKL5 beyond early development, underscore the potential for disease reversal in CDD, and suggest that a broad therapeutic time window exists for potential treatment of CDD-related deficits.

Introduction

Mutations in the X-linked gene encoding cyclin-dependent kinase-like 5 (CDKL5) are associated with a devastating neurodevelopmental syndrome known as CDKL5 deficiency disorder (CDD) (1–4). CDD is characterized by a constellation of phenotypes including intractable seizures, severe neurodevelopmental delay, intellectual disability, hypotonia, and autistic features (5, 6). The disorder predominantly afflicts young females heterozygous for mutations in *CDKL5*, but hemizygous male cases have also been reported (albeit at a markedly lower prevalence; refs. 6, 7). With an overall incidence of 1 per 42,000 live births, mutations in *CDKL5* are currently one of the most common genetic causes of epilepsy in children (8). Despite this strong genetic link, the pathogenesis of CDD remains unclear. Presently, there is no cure, and the limited treatment options available have focused on mitigating seizure burden using a variety of nonspecific anticonvulsants (5).

In 2012, the first knockout mouse model of CDD was generated and found to recapitulate several of the cardinal phenotypes of the human disease, including learning and memory impairments, motor deficits, and autistic-like behaviors (9). This line carries a deletion of *Cdkl5* exon 6, mimicking a reported CDD patient splice-site mutation resulting in exon 6 skipping and loss of full-length protein (10). Several additional knockout and knockin lines have since been generated with similar behavioral deficits, highlighting the reproducibility of CDD-related phenotypes in mice (11–13). Despite the multitude of CDD models, the time course of CDD pathogenesis, specific roles for CDKL5 in nervous system development versus maintenance, and reversibility of CDD-related phenotypes remain undetermined. Given the paucity of specific therapies, there is a pressing need to resolve these unknowns in order to develop targeted treatments.

CDKL5 is a serine-threonine kinase most highly expressed in forebrain neurons, where it is enriched at the neuronal postsynaptic density (PSD) (14–16). Recent work has identified microtubule-associated proteins as kinase targets, revealing a potential role for CDKL5 in regulating the microtubule network and morphology of neurons (17, 18). Indeed, previous studies in cultured hippocampal neurons have reported that shRNA-mediated knockdown of CDKL5 leads to an increased density of filipodia-like, or immature, spine protrusions that are consistent with observed reductions in the frequency of miniature excitatory postsynaptic currents (mEPSCs) (15). Loss of CDKL5 in mice results in reduced dendritic spine stability and density in the somatosensory cortex and visual cortex, but increased spine density in the hippocampus. Meanwhile, conditional knockout of CDKL5 selectively from forebrain excitatory neurons results in an increased spine density and frequency of mEPSCs within the hippocampal CA1 (12, 19–21). Conflicting results on these cellular phenotypes are likely due to regional differences within the brain as well as in vitro versus in vivo variability in neuronal activity and spine dynamics. Furthermore, the cell-autonomous versus non–cell-autonomous effects of CDKL5 loss on these reported phenotypes, particularly in light of developmental compensation that may occur with germline or cell type–specific *Cdkl5* deletion, remain unaddressed.

Clinical reports illustrating the early, postnatal onset of CDD symptomatology support a critical role for CDKL5 in the developing nervous system (5, 22). However, from a treatment perspective, it will be important to determine whether CDKL5 is also

Conflict of interest: The authors have declared that no conflict of interest exists.

Submitted: August 25, 2020; **Accepted:** August 5, 2021; **Published:** October 15, 2021.
Reference information: *J Clin Invest*. 2021;131(20):e143655.
https://doi.org/10.1172/JCI143655.

required for the maintenance of neurological function after development. Would transient treatment of CDKL5-related functional pathways during early postnatal life be sufficient to permanently mitigate disease? Conversely, can restoration of the kinase after critical periods of brain development reverse any CDD-related deficits? With recent advances in precision medicine highlighting promising treatment options for CDD patients in the future, it remains imperative to establish the temporal role of CDKL5 in neuronal development versus maintenance and the potential for symptom amelioration in patients who may have already passed a specific developmental time window (23).

To address these questions, we employed a genetic strategy to ablate *Cdkl5* expression in young adult, male mice and evaluated the functional significance of CDKL5 in the mature brain. We find that postdevelopmental deletion of *Cdkl5* results in behavioral and circuit deficits similar to those in germline knockout mice, suggesting that CDKL5 is indispensable in adulthood. We also demonstrate that loss of CDKL5 after the early stages of development alters neuronal dendritic spine morphology in a cell-autonomous manner, highlighting a critical role for this kinase in synaptic maintenance. In parallel, we have investigated the reversibility of CDD-associated symptoms by generating a conditional rescue mouse model that enables temporal control of *Cdkl5* reexpression at its endogenous locus. We find that the majority of CDD-related behavioral deficits, as well as aberrant NMDA receptor (NMDAR) signaling, are substantially mitigated with late restoration of CDKL5 expression in male mice. We believe these findings are the first to delineate a postdevelopmental requirement for CDKL5 and the first to demonstrate the potential for disease reversal in CDD. Importantly, our results uncover a broad therapeutic time window for numerous CDD-related deficits, supporting future therapeutic efforts aimed toward the treatment of CDD.

Results

Postdevelopmental loss of CDKL5 results in behavioral deficits similar to those in germline knockout mice. Several groups have previously reported on the early developmental expression pattern of CDKL5 across different tissues, demonstrating it to be most highly enriched in forebrain neurons (14, 22). We extended these studies by quantifying CDKL5 protein expression in the forebrain at different developmental time points, using knockout littermates to corroborate antibody specificity. We found that CDKL5 protein was detectable in forebrain tissues at P0, followed by a gradual increase and peak in expression around P14 (Figure 1A). After this postnatal peak, CDKL5 remained stably expressed in the forebrain throughout adulthood, suggesting that its function may not be exclusively limited to developmental processes (Figure 1A). This prompted us to investigate the necessity of CDKL5 in the maintenance of proper neurological function after development.

We crossed our previously reported *Cdkl5* floxed mouse line (*Cdkl5*^{fl}) to transgenic mice expressing a Cre-ERT2 fusion gene under the control of the human ubiquitin C promoter (UBC-CreER, hereafter referred to as CreER) (21). This line drives ubiquitous CreER expression and thereby allows for temporal control of gene deletion using tamoxifen (24). We delivered tamoxifen via oral gavage (0.3 mg/kg every other day for a total of 5 doses) to mice beginning at P42, the end of adolescence in C57BL/6 mice (25). This regimen resulted in successful ablation of CDKL5 protein expression to less than 5% of WT levels 1 week after tamoxifen delivery (Supplemental Figure 1; supplemental material available online with this article; https://doi.org/10.1172/JCI143655DS1). We then waited approximately 2 months (similarly to what was done in a previous adult knockout study of *Mecp2*) before evaluating behavioral phenotypes known to be disrupted in germline knockout animals in order to determine the functional impact of postdevelopmental loss of CDKL5 (9, 26). We focused on investigating hemizygous male mice to avoid potential confounds induced by mosaic expression of CDKL5 in heterozygous females as a result of random X chromosome inactivation. All experiments were performed on the following 3 groups: *Cdkl5*$^{fl/Y}$; +/+ (floxed), *Cdkl5*$^{+/Y}$; CreER/+ (CreER), and *Cdkl5*$^{fl/Y}$;CreER/+ (AKO), where all genotypes received tamoxifen in order to minimize potential variability introduced upon tamoxifen administration (27). Post hoc CDKL5 protein quantification in all experimental mice confirmed a nearly complete loss of CDKL5 protein in the brains of AKO animals, but not floxed or CreER littermate controls (Figure 1B).

We found that AKO mice exhibited motor and anxiety-related impairments similar to those of *Cdkl5* germline knockout animals. AKO mice spent significantly more time in the open arm of the elevated zero maze, which was suggestive of decreased anxiety-related behaviors (Figure 1C and Supplemental Figure 2), and were hyperactive during an open-field test (Figure 1D and Supplemental Figure 2). They also recapitulated several of the autistic-like features observed in germline knockout models of CDD, such as reduced time sniffing and direct interaction with a novel stimulus mouse in the 3-chambered social choice test (Figure 1, E and F, and Supplemental Figure 2) as well as increased repetitive grooming and digging behaviors (Figure 1G) when compared with littermate floxed and CreER controls. Moreover, AKO mice displayed significantly impaired contextual- and cue-dependent memory in a Pavlovian fear-conditioning paradigm when compared with floxed and CreER controls, though working memory measured by the Y maze assay appeared unaffected (Figure 1, H and I, and Supplemental Figure 2). Interestingly, AKO mice showed enhanced motor coordination on the rotarod assay, with a significantly increased latency to fall from an accelerating, rotating rod and no hind limb clasping when compared with floxed and CreER controls (Figure 1J and Supplemental Figure 2). This is contrary to the *Cdkl5* germline knockout phenotype in which mice exhibit significantly impaired motor coordination. Importantly, we did not find any significant differences across all examined behavioral domains between floxed and CreER controls, suggesting that the presence of the CreER allele alone does not induce any abnormal phenotypes. In summary, although two documented germline knockout phenotypes were not recapitulated in AKO mice, our results highlight several major behavioral domains disrupted upon adult loss of CDKL5, supporting an indispensable role for CDKL5 in the postdeveloped brain.

Postdevelopmental loss of CDKL5 results in disruption of low-frequency event–related neuronal oscillations. Auditory or visual event–related potentials (ERPs) have been increasingly leveraged as biomarkers for sensory information–processing deficits in both patients and animal models of various neurodevelopmental disorders (28). We previously reported that germline loss of CDKL5

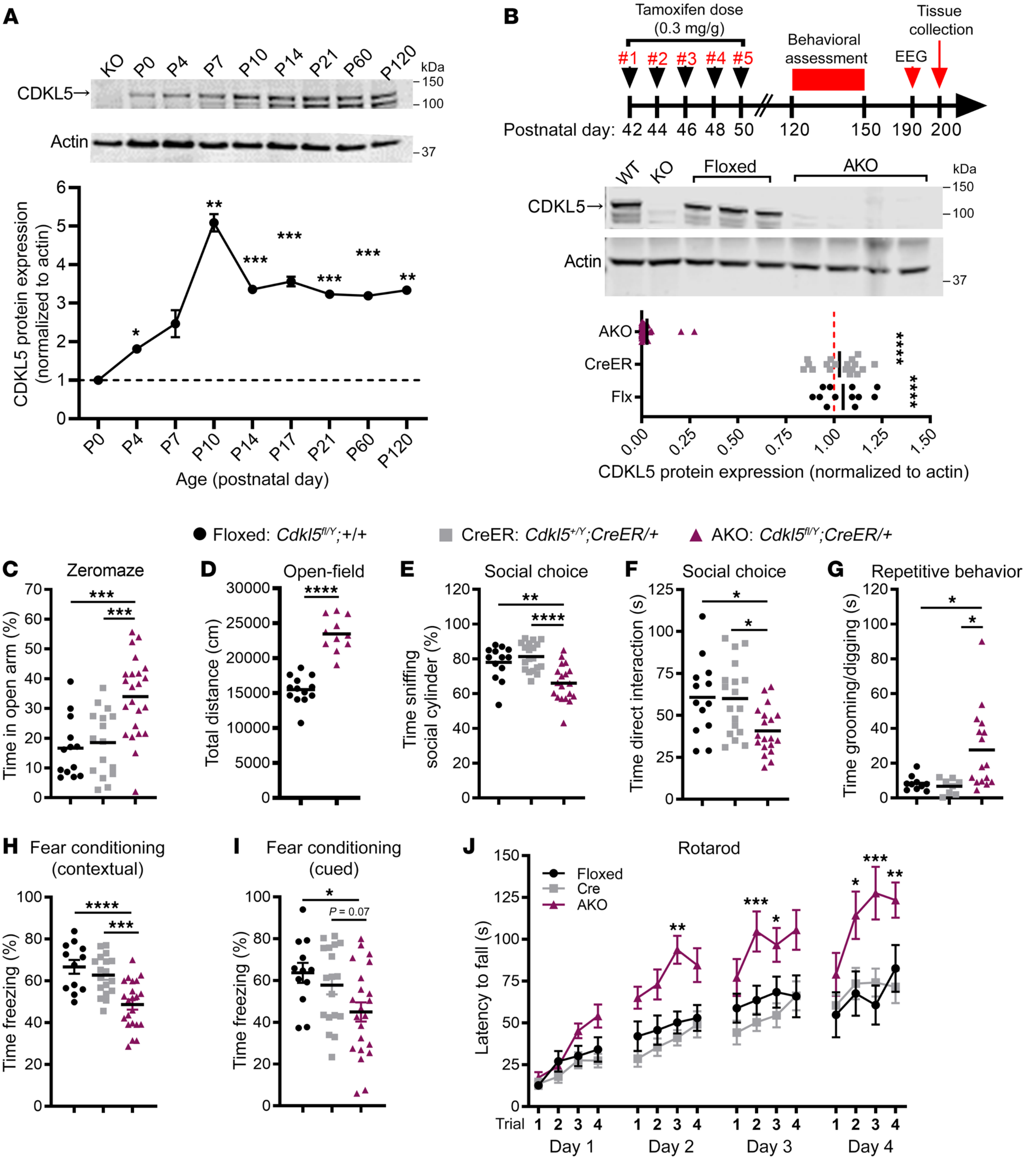

Figure 1. Postdevelopmental loss of CDKL5 disrupts multiple behavioral domains in mice. (**A**) Top: representative Western blot showing CDKL5 and actin protein expression from forebrain tissues of WT mice across multiple ages, where knockout tissue was referenced for antibody specificity; bottom: quantification of CDKL5 protein, normalized to actin, and plotted relative to P0 levels (mixed effects analysis; *n* = 4). (**B**) Top: tamoxifen and experimental schedule; bottom: representative Western blot and quantification of CDKL5 protein expression in forebrain tissues of all experimental mice. Values were normalized to actin and plotted relative to CreER-only CDKL5 levels. (**C**) AKO mice spend significantly more time in the open arm of the elevated zero maze assay compared with floxed and CreER littermates. (**D**) AKO mice travel significantly more distance than floxed littermates in the open-field assay. (**E**) AKO mice spend significantly less time than floxed and CreER littermates sniffing and (**F**) directly interacting with a novel stimulus mouse during the 3-chambered social choice test. (**G**) AKO mice spend more time grooming or digging in a home cage–like environment than floxed and CreER littermates. (**H**) AKO mice spend significantly less time freezing compared with floxed and CreER littermates when returned to the fear-conditioning testing chamber (contextual) and (**I**) upon hearing the footshock-associated tone (cue). (**J**) AKO mice take significantly more time to fall from an accelerating, rotating rod than floxed and CreER littermates. For all panels, floxed, *n* = 13; CreER, *n* = 19; AKO, *n* = 23 where all genotypes received tamoxifen. One-way ANOVA test with Holm-Šidák post hoc test, except as follows: open field, unpaired, 2-tailed *t* test; 3-chambered social choice assay and repetitive behaviors, Kruskal-Wallis test with Dunn's multiple-comparison test; rotarod, 2-way repeated measures ANOVA with Šidák's multiple-comparison test. *$P < 0.05$, **$P < 0.01$, ***$P < 0.001$, ****$P < 0.0001$. Data are represented as mean ± SEM. Full-scan Western blots of all samples are available in the supplemental material.

resulted in disrupted auditory-evoked ERPs recorded from the hippocampus, reflecting an impairment in neural circuit activity (9). We thus measured sensory-evoked ERPs in the hippocampus of AKO mice in response to an auditory cue. These assessments were performed on nonanesthetized, freely mobile mice and were not confounded by the motor and cognitive deficits observed in our CDD models. We found that AKO animals displayed an aberrant ERP waveform with a significantly decreased amplitude of the canonical N1 (negative) and P2 (positive) polarity peaks as well as a significantly increased latency in the P2 polarity peak; this is similar to what occurred in *Cdkl5* germline knockout animals (Figure 2A). The amplitude and latency of these ERP polarity peaks are thought to reflect the strength and timing of cognitive processes, suggesting that adult loss of CDKL5 also impairs sensory information processing in conjunction with compromised behavioral functions.

Time-frequency analysis of these ERPs in the hippocampus also demonstrated reduced oscillatory strength specifically in the low-frequency δ (2–4 Hz), θ (4–8 Hz), and α (8–12 Hz) oscillations, but no differences in the high-frequency β (12–30 Hz), low γ (γ_{low}) 30–50 Hz), and high γ (γ_{high}) 70-140 Hz) oscillations in AKO mice relative to floxed littermate controls (Figure 2, B and C). Similarly, event-related phase locking (measured by the phase-locking factor [PLF]), which reflects the reliability and sensitivity of circuit communication, was also significantly decreased in AKO mice compared with floxed littermate controls selectively in the low-frequency δ and θ (Figure 2, B and C). Notably, EEG studies in children with autism spectrum disorder (ASD) have shown selective deficits in low-frequency δ, θ, and α oscillations, suggesting similar neural network defects in CDD and related syndromic ASDs (28). Together, these results indicate that adult loss of CDKL5 leads to hippocampal network alterations similar to those reported in germline knockout animals and that CDKL5 is required for the maintenance of proper signaling within this circuit throughout life.

CDKL5 is required for the maintenance of dendritic spine morphology. Previous studies have reported that loss of CDKL5 leads to aberrant dendritic spine stability/morphology and perturbed mEPSCs, suggesting an important role for CDKL5 in neuronal synapse maturation (12, 15, 16, 19–21). The extent to which CDKL5 regulates the formation and/or maintenance of these highly dynamic compartments, however, remains unknown. Ablating CDKL5 expression selectively in adulthood provided us with a unique opportunity to examine the consequences of CDKL5 loss on neuronal morphology independently of developmental confounds or homeostatic compensatory mechanisms that can arise during development, especially since previous studies have documented age-dependent changes in spine morphology (29).

Given that our prior work has demonstrated a critical role for CDKL5 in the hippocampus along with the fact that CDKL5 is highly enriched in excitatory cells of this circuit, we directed our initial studies to pyramidal neurons of the hippocampal CA1 (9, 13, 21). We examined the effects of germline and postdevelopmental loss of CDKL5 on dendritic spines of pyramidal neurons in this region by crossing either *Cdkl5* knockin mice ($Cdkl5^{R59X}$, R59X, which results in early truncation and loss of function) or AKO mice to a Thy1-GFPm reporter line (13, 30). This sparse reporter allele allows for in vivo visualization of pyramidal neurons in their entirety and subsequent analysis of dendritic spine density and morphology (30). We found that dendritic spine density was not significantly altered on either basal or apical dendritic trees of CA1 pyramidal neurons between CDKL5 R59X knockin ($Cdkl5^{R59X/Y}$; Thy1-GFPm/+) and WT littermate ($Cdkl5^{+/Y}$; Thy1-GFPm/+) animals, or between AKO ($Cdkl5^{fl/Y}$:CreER/+; Thy1-GFPm/+) mice and floxed littermate controls ($Cdkl5^{fl/Y}$; +/+; Thy1-GFPm/+) arguing that loss of CDKL5 during either development or adulthood does not significantly alter dendritic spine density in vivo in the hippocampal CA1 (Supplemental Figure 3).

Aside from spine density and turnover, previous work in cultured neurons and *Cdkl5*-knockout animals has also proposed an altered spine morphology in CDD models (12, 15, 19–21). We thus evaluated various components of dendritic spine morphology in an in vivo setting using reconstruction and analysis of the 3D confocal image stacks taken for spine-density quantifications. We found that, on average, spine length was significantly increased on both basal and apical dendrites of pyramidal CA1 neurons of AKO mice compared with floxed controls (Figure 2, E and I). This phenotype, coupled to a trending decrease in spine head diameter, may reflect an altered spine maturity and/or synaptic strength (29, 31 and Figure 2, F, G, J, and K). Given that the total density of dendritic spines remained unchanged (Figure 2, D and H), these findings suggest an increased representation of morphologically distinct spines on both apical and basal trees of CA1 pyramidal neurons in AKO mice, resembling similar findings seen upon loss of CDKL5 in cultured hippocampal neurons (15).

Our adult knockout allows for an evaluation of neuronal morphological deficits resulting from CDKL5 loss in vivo independently of developmental confounds. However, it remained uncertain whether this spine phenotype was indeed a cell-autonomous effect of CDKL5 loss or a compensatory phenotype due to ablation of CDKL5 in every cell. Sparse, conditional deletion isolates the single-neuron consequences of CDKL5 loss while also bypassing pre- versus postsynaptic effects of mutant cells on spine dynamics. We therefore performed a conditional, sparse deletion of CDKL5 in adult mice by crossing *Cdkl5* floxed mice to SLICK transgenic mice. The single-neuron labeling with inducible Cre-mediated knockout (or SLICK) technique utilizes two copies of the Thy1 promoter to simultaneously drive sparse expression CreER and yellow fluorescent protein (YFP), thereby allowing for conditional knockout and simultaneous labeling of individual neurons to assess cell-autonomous–driven morphology (32). $Cdkl5^{fl/Y}$; SLICK/+ mice and WT controls ($Cdkl5^{+/Y}$; SLICK/+) received tamoxifen beginning at P42, and their spine morphology was subsequently analyzed at P70. We found that sparse, conditional deletion of CDKL5 in adulthood amplified the increased spine length of both apical and basal dendritic spines on CA1 pyramidal neurons seen in AKO animals (Supplemental Figure 4, B and F). We also observed a significantly decreased spine head diameter and decreased spine volume, on average, of basal and apical CA1 dendritic spines on knockout neurons in comparison with WT control neurons (Supplemental Figure 4, C, D, G, and H). Notably, the spine dimensions reported in Supplemental Figure 4 are much smaller than expected due to the suboptimal YFP signal of the SLICK reporter line during image reconstruction. Despite this discrepancy, we observed a reproducible, genotype-dependent effect on spine morphology. Again, there was no change in spine density on either apical or basal dendritic arbors

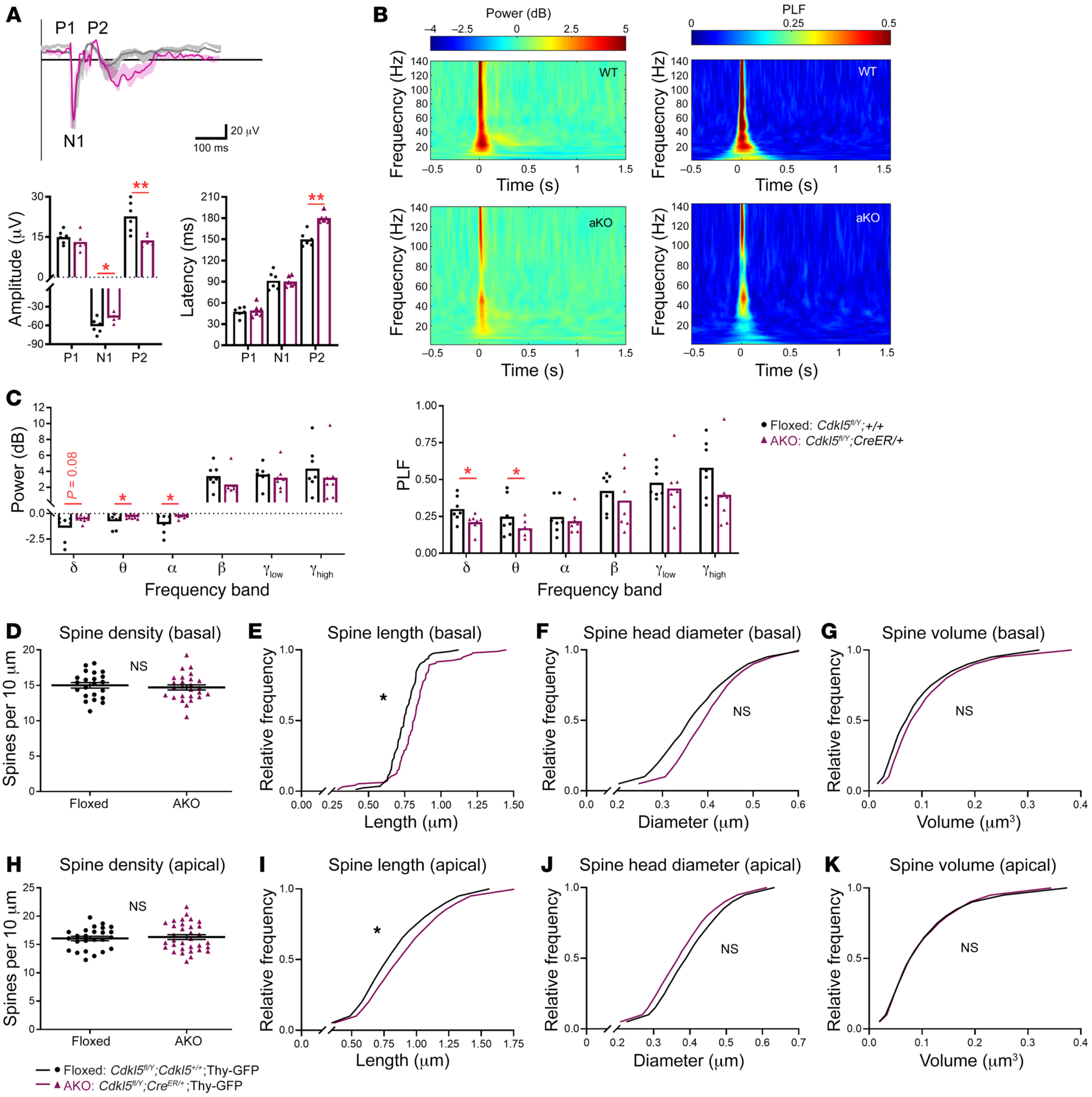

Figure 2. Postdevelopmental loss of *Cdkl5* disrupts hippocampal ERPs and dendritic spine morphology. (**A**) Top: grand-average hippocampal CA1 ERP wave form following presentation of auditory stimuli in *Cdkl5*$^{fl/Y}$; +/+ (floxed; gray) and *Cdkl5*$^{fl/Y}$:CreER/+ (AKO; purple) mice. Traces represent mean amplitude ± SEM. Characteristic polarity peaks P1, N1, and P2 in floxed control are labeled. Scale bars: 100 ms (horizontal); 20 mV (vertical). Bottom: quantification of the amplitude and latency of ERP P1, N1, and P2 peaks (unpaired, 2-tailed *t* test). (**B**) Time-frequency plots showing changes in event-related power (left) and PLF (right) following auditory stimulus with no alterations in baseline EEG power. Color represents mean power/PLF, where warmer colors correspond to increased power/PLF and cooler colors correspond to decreased power/PLF relative to prestimulus baseline. (**C**) Changes in event-related mean power (top) and PLF (bottom) averaged across δ (2–4 Hz), θ (4–8 Hz), α (8–12 Hz), β (12–30 Hz), γ_{low} (30–50 Hz), and γ_{high} (70–140 Hz) oscillation frequencies demonstrate a selective disruption of power and phase locking in the low-frequency oscillations in AKO mice over floxed littermate controls (unpaired, 2-tailed *t* test). Data are represented as mean ± SEM. *n* = 7 floxed and *n* = 7 AKO for all ERP experiments. (**D**) *Cdkl5*$^{fl/Y}$:CreER/+; Thy1-GFPm/+ (AKO) mice show no significant change in spine density on either basal or (**H**) apical dendritic arbors of CA1 pyramidal neurons compared with *Cdkl5*$^{fl/Y}$; +/+; Thy1-GFPm/+ (floxed) littermate controls. AKO neurons have increased spine length compared with floxed littermate control neurons on both (**E**) basal and (**I**) apical dendritic arbors. Spine head diameter (**F**, basal; **J**, apical) and spine volume (**G**, basal; **K**, apical) were not significantly different between AKO and floxed neurons. For all spine analyses, basal, *n* = 22 cells/8 mice for floxed, *n* = 30 cells/7 mice for AKO; apical, *n* = 25 cells/8 mice for floxed, *n* = 36 cells/7 mice for AKO. Linear mixed effects analysis. $^*P < 0.05$, $^{**}P < 0.01$.

between *Cdkl5* sparse knockout and WT control neurons (Supplemental Figure 4, A and E).

Taken together, these results demonstrate an increased proportion of filipodia-like dendritic spines on CA1 pyramidal neurons of the hippocampus with loss of *Cdkl5* and highlight a key role for CDKL5 in the maintenance of dendritic spine morphology in a cell-autonomous manner. Recent studies have suggested a role for CDKL5 in microtubule dynamics through its direct phosphorylation of microtubule-associated proteins such as end-binding 2 (EB2) protein (17). We found that phosphorylation of endogenous EB2 Ser222 (pS222) was significantly reduced in forebrain tissues of AKO mice to a magnitude similar to that observed in CDKL5 R59X knockin mice (Supplemental Figure 5). This suggests that this microtubule-associated substrate remains modulated by CDKL5 in adulthood and that similar microtubule network disruptions may occur upon postdevelopmental loss of CDKL5. These morphological deficits, coupled with an impaired regulation of EB2, represent a potential cellular basis for the behavioral and circuit phenotypes exhibited by AKO animals.

Postdevelopmental restoration of CDKL5 rescues numerous CDD-related behavioral deficits. Our present findings support the hypothesis that postdevelopmental loss of CDKL5 induces phenotypes similar to those of germline knockout. However, the reversibility of CDD-associated symptoms remains unknown in the field, especially since the disorder presents very early in life. Given that CDD patients do not normally experience neurodegeneration, the viability of mutant neurons in CDD patients opens up the prospect that reexpression of CDKL5 (or therapeutic intervention) may restore CDKL5-dependent signaling pathways and thereby alleviate some of the disorder phenotypes. If a critical time window of CDKL5 function does exist, then delayed treatment (or gene replacement) may have little effect or even contravening outcomes in a system that has partially compensated for its loss.

To address this, we created a mouse line in which endogenous *Cdkl5* gene transcription is terminated by the insertion of a *loxP*-flanked transcriptional STOP cassette and in which physiological levels of *Cdkl5* expression can be restored upon Cre-mediated cassette deletion (*Cdkl5*^{STOP}, hereafter referred to as STOP; Figure 3A). This is particularly relevant as human genetic studies have reported that duplication of *CDKL5* is associated with neurological impairments (33). Western blot analysis of STOP mice across multiple surveyed brain regions, and using 3 different CDKL5 antibodies, demonstrated no observable CDKL5 protein levels (Supplemental Figure 6A and Supplemental Figure 7). These results resemble the level of ablation of CDKL5 protein expression across multiple mouse models of CDKL5 deficiency (Supplemental Figure 6A). A preliminary characterization of STOP mice highlighted phenotypes similar to those of *Cdkl5* mutant mice by P42, the age at which we began tamoxifen administration (Supplemental Figure 6). When we crossed this conditional rescue allele to a tamoxifen-inducible Cre mouse line (UBC-CreER), we detected a small but significant amount of CDKL5 protein in cortical tissues of STOP;CreER mice, but not STOP-only littermates, amounting to approximately 19% of WT levels (Supplemental Figure 8, A and B). The extent of leaky *Cdkl5* expression varied in different brain regions, with the highest occurring in the cortex of STOP;CreER mice (Supplemental Figure 7). This is likely due to unexpected CreER translocation into the nucleus even in the absence of tamoxifen, with recombination occurring in approximately 19% of cells that subsequently express endogenous levels of CDKL5 in the cortex. Despite this, a comprehensive examination of behavioral phenotypes across naive WT, UBC-CreER (CreER), STOP, and STOP;CreER animals demonstrated that STOP-only and STOP;CreER animals were indistinguishable from one another prior to tamoxifen administration and recapitulated numerous phenotypes previously reported for *Cdkl5* knockout mice when compared with WT and CreER-only littermates (Supplemental Figure 8, C–P). These data suggest that a low percentage of cells expressing CDKL5, such as up to 19% of cells in the cortex, does not significantly alter behavioral phenotypes of STOP mice, consistent with the literature showing that heterozygous females with approximately 50% of cells expressing CDKL5 typically develop CDD (5).

We next delivered tamoxifen to 4 experimental groups of mice: *Cdkl5*$^{+/Y}$*; +/+* (WT), CreER, *Cdkl5*$^{STOP/Y}$*; +/+* (STOP), and *Cdkl5*$^{STOP/Y}$;CreER/+ (rescue [Res]) beginning at P42 using the same regimen applied in our adult knockout experiments (0.3 mg/kg^{-1} every other day for a total of 5 doses). We observed substantial restoration of CDKL5 protein expression in forebrain tissues of Res mice, but not STOP mice, that was comparable to that of WT and CreER-only littermate controls within 2 weeks of tamoxifen delivery. Unexpectedly, we noticed significant lethality at this dosage selectively in Res mice, but not WT, CreER, or STOP animals (Supplemental Figure 9). These findings suggest there may be toxicity associated with rapid *Cdkl5* reactivation, even at endogenous levels of CDKL5 expression. A previous rescue study using a mouse model of Rett syndrome also reported significant lethality with rapid reexpression of *Mecp2*. This effect was mitigated by a more gradual induction protocol using a slower regimen of tamoxifen (34). We similarly adjusted our tamoxifen administration protocol and found that a more gradual *Cdkl5* activation (1 tamoxifen dose of 0.3 mg/kg every week for a total of 3 weeks, followed by 2 booster treatments) was able to eliminate this toxicity while restoring CDKL5 expression to nearly WT levels (Figure 3B and Supplemental Figure 9). Consequently, we adhered to this gradual *Cdkl5* activation protocol for subsequent rescue experiments. Remarkably, phosphorylation of EB2 Ser222 was also restored to control levels upon adult reversal of *Cdkl5* expression, highlighting that CDKL5-dependent signaling pathways are likely rescued with tamoxifen delivery and *Cdkl5* reexpression (Figure 3B).

Using this gradual gene-reversal strategy, we next examined the extent to which late restoration of CDKL5 expression could mitigate CDD-related behavioral deficits. We again administered tamoxifen to a cohort of CreER, STOP, and Res littermates from P42 to P60, the age at which most behavioral deficits have arisen in STOP mice (Supplemental Figure 6). Beginning at P120, we evaluated multiple behavioral domains known to be disrupted in *Cdkl5* germline and adult knockout animals. Res animals showed improvement over STOP littermates in hyperactivity and anxiety-related behaviors. STOP mice spent significantly more time exploring the open arm of the elevated zero maze in comparison with CreER-only controls, suggestive of decreased anxiety (Figure 3C). However, restoration of *Cdkl5* from 6 weeks of age resulted in a significant decrease in open-arm time compared with that of STOP mice, with Res animals behaving comparably to CreER

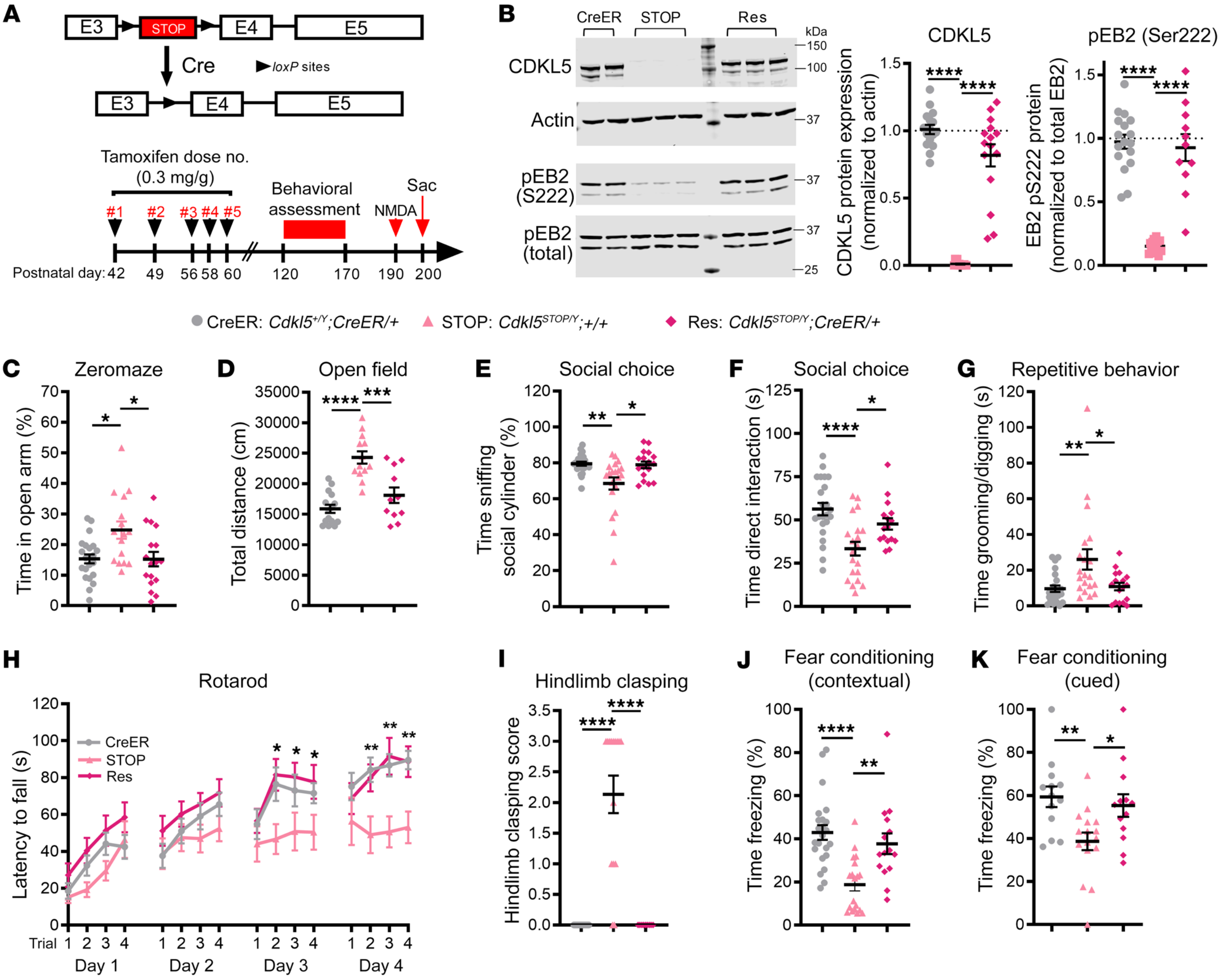

Figure 3. Adult restoration of *Cdkl5* expression rescues CDD-associated behavioral deficits. (**A**) Top: *Cdkl5*^{STOP} mice carry a *loxP*-flanked transcriptional STOP cassette in the endogenous *Cdkl5* that can be removed in the presence of CreER; bottom: tamoxifen and experimental schedule. (**B**) Left: representative Western blot of CDKL5, actin, pEB2(Ser222), and total EB2 protein levels in CreER, STOP, and Res forebrain tissues. Right: quantification of CDKL5 and pEB2(Ser222) protein levels for all genotypes normalized to actin and total EB2 levels, respectively. (**C**) STOP mice spend significantly more time than Res and CreER littermates in the open arm of the elevated zero maze assay. (**D**) STOP mice travel significantly more distance in the open-field assay than CreER and Res littermates. (**E**) STOP mice spend significantly less time sniffing and (**F**) directly interacting with a stimulus mouse during the 3-chambered social choice test compared with CreER and Res littermates. (**G**) STOP mice spend significantly more time grooming and digging in a home cage-like environment compared with CreER and Res littermates. (**H**) STOP mice take significantly less time to fall from an accelerating, rotating rod than CreER and Res littermate controls. (**I**) STOP mice, but not CreER or Res mice, present with hind limb clasping behaviors. (**J**) STOP mice freeze significantly less compared with CreER and Res littermates when returned to the fear-conditioning testing chamber (contextual) and (**K**) upon hearing the testing tone (cue). For all panels, CreER, *n* = 23; STOP, *n* = 20; Res, *n* = 17 where all genotypes received tamoxifen. One-way ANOVA test with Holm-Šidák post hoc test, except 3-chambered social choice assay and repetitive behaviors: Kruskal-Wallis test with Dunn's multiple-comparison test; rotarod: 2-way repeated measures ANOVA with Šidák's multiple-comparison test. $*P < 0.05$; $**P < 0.01$; $***P < 0.001$; $****P < 0.0001$. Data are represented as mean ± SEM. Full-scan Western blots of all samples are available in the supplemental material.

controls (Figure 3C and Supplemental Figure 10). STOP mice also moved significantly more over the course of 1 hour in an open-field test when compared with CreER-only controls, whereas Res mice exhibited activity levels closer to those of CreER control littermates (Figure 3D and Supplemental Figure 10). Postdevelopmental restoration of CDKL5 also ameliorated several of the autistic-like phenotypes frequently reported upon *Cdkl5* deletion. During the 3-chambered social choice assay, Res animals spent amounts of time similar to those of CreER-only controls sniffing the social cylinder and directly interacting with a novel stimulus mouse, while STOP mice spent significantly less time sniffing the social cylinder and directly interacting with a novel stimulus mouse, suggestive of decreased sociability (Figure 3, E and F, and Supplemental Figure 10). STOP mice also exhibited aberrant repetitive behaviors, illustrated by an increased time spent grooming/digging in a home cage-like environment when compared with CreER controls, whereas Res mice displayed control-level grooming/digging behaviors (Figure 3G).

Similarly to other *Cdkl5* knockout models, STOP mice recapitulated impaired motor learning on the rotarod assay, as demonstrated by a decreased latency to fall from an accelerating, rotating rod as well as a penetrant hind limb clasping phenotype. Postdevelopmental rescue of CDKL5 significantly ameliorated these motor deficits, with Res mouse performance on the rotarod assay comparable to that of littermate CreER-only controls and no hind limb clasping present in any of the 17 Res animals tested (Figure 3, H and I). Finally, normal context- and cue-dependent learning and memory were also restored to near-control levels in Res animals, while STOP mice displayed significant impairment in both of these memory domains (Figure 3, J and K, and Supplemental Figure 10). Interestingly, working memory, as measured by spontaneous alternations during the Y maze assay, was not significantly improved in Res animals when compared with STOP-only littermate mice (Supplemental Figure 10). However, total activity during the Y maze assay (measured by the total number of alternations and total distance traveled) was significantly restored to CreER control levels in Res animals, which aligns with the ameliorated hyperactivity phenotype illustrated by the open-field test (Supplemental Figure 10). Collectively, these findings support the idea that postdevelopmental restoration of CDKL5 is sufficient to reverse or ameliorate a majority of loss-of-function behavioral impairments. The hyperactivity, anxiety-related phenotypes, autistic-like behaviors, motor impairments, and learning and memory deficits in CDD mice appear to remain amenable to postdevelopmental restoration of CDKL5 expression.

Postdevelopmental restoration of CDKL5 abrogates NMDA-induced hyperexcitability and aberrant NMDAR-mediated synaptic responses. The rescue of behavioral phenotypes upon reexpression of endogenous *Cdkl5* in young adult mice raises the possibility that the molecular and cellular deficits caused by loss of CDKL5 are also reversible. To investigate this, we focused on the aberrant NMDAR signaling phenotypes previously found to be altered in *Cdkl5* knockout and knockin mice. Specifically, CDD mouse models display an increase in the ratio of NMDA-mediated to α-amino-3-hydroxy-5-methyl-4-isoxazolepropionic acid–mediated (AMPA-mediated) excitatory postsynaptic current (NMDA/AMPA EPSC ratio) in the CA1 region of the hippocampus that correlates with an increased susceptibility to NMDA-induced seizures (13, 35). The NMDA-mediated synaptic responses in CDD mouse models also display larger decay times, suggestive of a higher contribution of GluN2B-containing NMDARs.

Consistent with our previous studies in *Cdkl5* knockout and CDKL5 R59X knockin models, we found that the levels of membrane-associated GluN2B in PSD fractions purified from STOP mice were significantly elevated compared with those of littermate controls, but detected no change in several other major ionotropic glutamate receptor subunits, such as GluA1, GluA2, and GluN2A (Figure 4, A–E). Correspondingly, STOP mice also recapitulated the enhanced susceptibility to NMDA-induced seizures shown in other *Cdkl5* knockout lines (Figure 4F and refs. 13, 35). These phenotypes were further supported by an increase in the NMDA/AMPA ratio onto CA1 pyramidal neurons of the hippocampus. Additionally, the NMDA-mediated currents displayed a significantly larger decay time constant, highlighting NMDAR signaling deficits similar to those of other CDD models (Figure 4, G–I, and ref. 35). Remarkably, we found that late restoration of *Cdkl5* expression was able to reverse these NMDAR synaptic phenotypes. Postdevelopmental reversal of *Cdkl5* expression using our established tamoxifen regimen beginning at P42 restored GluN2B expression to CreER-only levels, and consistently attenuated the enhanced susceptibility to NMDA-induced seizures exhibited by STOP-only mice (Figure 4, A–F). Furthermore, the ratio of NMDA/AMPA currents and NMDAR-current kinetics were rescued as a result of restoring *Cdkl5*, suggesting reestablishment of control-level NMDAR subunit composition (Figure 4, G–I). Together, these findings demonstrate that late restoration of CDKL5 expression attenuates the aberrant NMDAR signaling deficits in the hippocampus that result from CDKL5 loss, underscoring the reversibility of molecular and synaptic signaling deficits present in CDD models.

Discussion

Several mouse models of CDD have been characterized to date, and although they recapitulate many of the hallmark phenotypes of the human disorder, it remains unclear whether these phenotypes are a consequence of detrimental changes exclusively accumulating in the developing nervous system or are similarly inducible upon loss of CDKL5 in mature neurons. Furthermore, from a therapeutic perspective, it is imperative to determine the reversibility of CDD-related deficits, particularly after the early stage of brain development, and to delineate the temporal requirement of CDKL5 action needed to establish as well as maintain proper neurological function. Prior to this study, it remained unknown whether CDD symptomatology was reversible and whether a critical developmental time window was required for treatment. Our temporal knockout and temporal rescue experiments address these questions, at least in male mouse models, and constitute a seminal foundation for future endeavors to dissect the pathogenic origins of CDD and design effective therapeutic strategies.

Postdevelopmental requirement of CDKL5. Our findings demonstrate that multiple behavioral and circuit phenotypes in knockout mouse models of CDD are recapitulated following deletion of *Cdkl5* at 6 weeks of age. Specifically, postdevelopmental loss of CDKL5 resulted in similar deficits in anxiety-related behaviors, locomotion, sociability, repetitive behaviors, context- and cue-dependent learning and memory, and auditory-evoked ERPs, as previously reported in germline knockout mice (9). In parallel, postdevelopmental restoration of *Cdkl5* expression ameliorates most of these loss-of-function deficits in male mice, suggesting that the underlying circuitry critical for many of the aforementioned behavioral domains is amenable to later kinase restoration. Thus, CDKL5 appears to be required not only during development, but also in adulthood, suggesting that chronic, lifelong treatment of CDD will likely be required.

Interestingly, working memory, as measured via spontaneous alternations in a Y maze assay, was not significantly affected by postdevelopmental loss or restoration of CDKL5 expression, demonstrating that CDKL5 does function critically in early development. The fact that working memory remains unaffected in AKO mice despite concomitant motor and anxiety-related deficits suggests that similar impairments in *Cdkl5* germline knockout animals are not simply a byproduct of other phenotypic confounds.

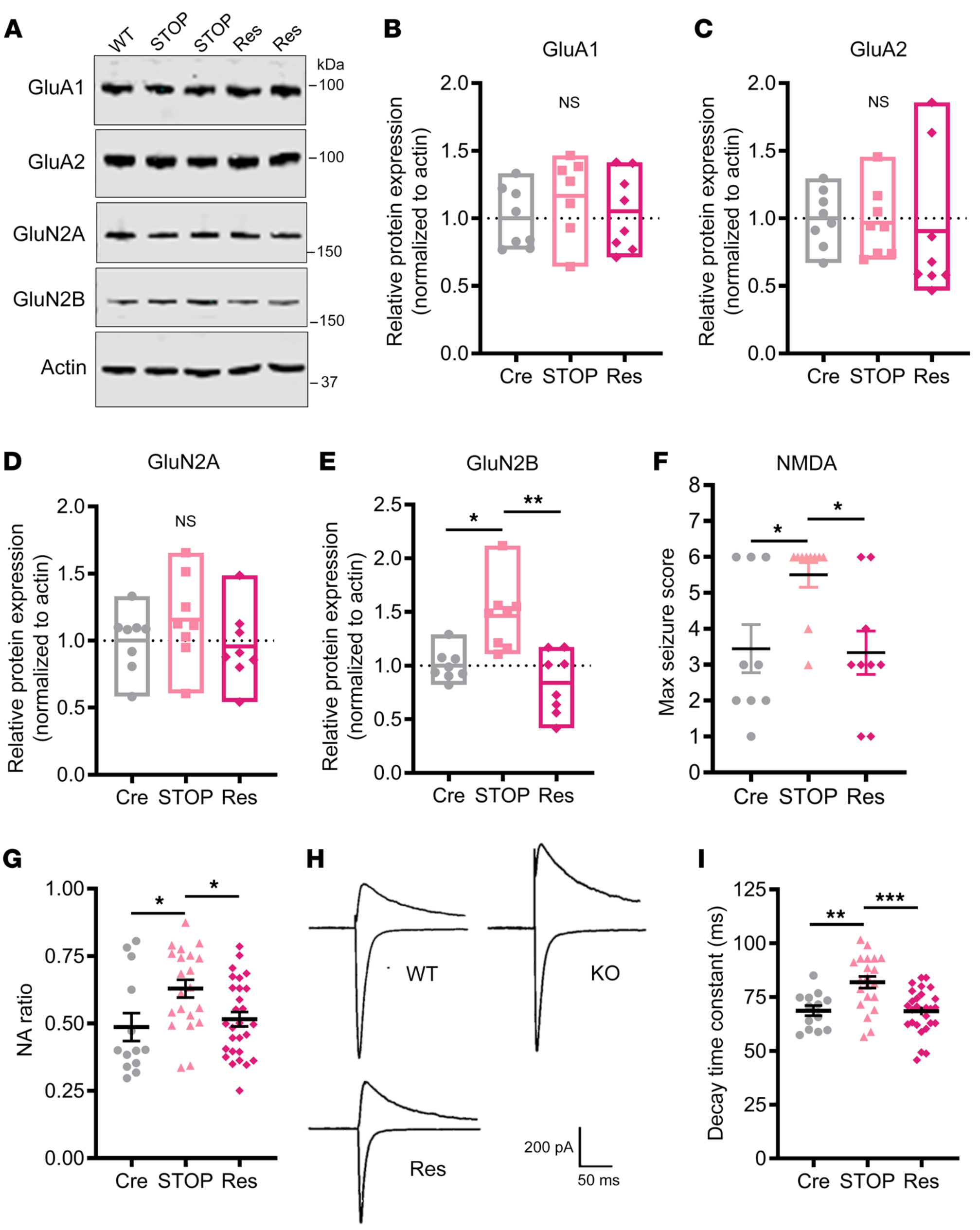

Figure 4. Adult restoration of CDKL5 abrogates aberrant NMDAR-mediated synaptic responses. (**A**) Representative Western blots showing several major ionotropic glutamate receptor subunits from PSD membrane fractions in CreER, STOP, and Res mice. (**B**–**E**) STOP, but not Res, mice show a selective increase in levels of GluN2B, a major subunit of the NMDAR, compared with CreER littermate controls (*n* = 8 per genotype). (**F**) STOP, but not Res, mice show a significantly increased susceptibility to NMDA-induced seizures compared with CreER littermate controls (CreER, *n* = 9; STOP, *n* = 10; Res, *n* = 9). (**G**–**I**) STOP, but not Res, mice show an increased ratio of NMDA-mediated to AMPA-mediated synaptic responses (NA) in the hippocampal CA1 (**G**) concomitant with a significantly larger decay time constant of NMDAR-mediated EPSCs (**I**) when compared with CreER littermates. Representative traces are shown in **H**. This suggests a higher contribution of GluN2B-containing NMDARs in STOP mice and an attenuation of aberrant NMDAR signaling deficits in Res mice. For all panels, Kruskal-Wallis test with Dunn's multiple-comparison test, except for **G** and **I**, which used 1-way ANOVA with Tukey's multiple-comparison test. $^{*}P < 0.05$; $^{**}P < 0.01$; $^{***}P < 0.001$. Data are represented as mean ± SEM. Full-scan Western blots of all samples are available in the supplemental material.

In contrast, context- and cue-dependent memory retrieval appear to be sensitive to both postdevelopmental loss and restoration of CDKL5, owing to their likely distinct circuit origins from working memory (36). The significant hyperactivity reported across CDD mouse models represents an important caveat to consider during the interpretation of behavioral assays.

Surprisingly, postdevelopmental knockout of *Cdkl5* resulted in markedly enhanced motor learning in contrast with the impaired motor learning and coordination reported in germline knockout animals. Although motor coordination and learning are associated with proper cerebellar functioning, CDKL5 has low expression in this brain region, suggesting additional circuitry may drive this phenotype (9). Furthermore, a recent study in *Cdkl5* knockout mice utilizing AAV-*CDKL5* vectors expressed in the hind brain (including cerebellum), but not forebrain, reported only partial rescue of motor coordination deficits on the rotarod assay, pointing to an extracerebellar function of CDKL5 in driving these motor phenotypes (37). Notably, the basal ganglia, where CDKL5 is highly expressed (Supplemental Figure 7), also play a known role in motor control and learning and have been highlighted as a common node for ASD pathophysiology (38). How loss of CDKL5 in adulthood leads to improved motor coordination and learning remains uncertain but represents an interesting future avenue to investigate temporally distinct influences of CDKL5 loss on the same behavioral output.

Late CDKL5 restoration yields therapeutic insights. Previous studies have applied the concept of late gene reversal in rodents to attempt phenotypic rescue in various models of neurodevelopmental disorders (34, 39, 40). Late restoration of *Mecp2* expression in knockout mice has been reported to alleviate impairments associated with Rett syndrome, and adult restoration of *Shank3* is capable of rescuing selective autistic-like phenotypes (34, 39). Meanwhile, a recent finding reported that adult restoration of the SynGAP protein selectively improved electrophysiological measures of memory and seizures (40). CDD, however, is distinct from these and other autism spectrum and neurodevelopmental disorders in that it is characterized by early onset features within the first few weeks after birth as opposed to a developmental regression after the first few years of life (41, 42). Thus, our temporal reversal findings provide a development over these previous studies and demonstrate the potential for treatment of neurological symptoms despite the lack of a relatively stable early postnatal period. We also found that postdevelopmental restoration of *Cdkl5* expression ameliorated multiple behavioral deficits related to CDD in hemizygous male mice, rather than a few selective behavioral domains, as was reported in previous reversal studies. These findings raise the possibility that the CDD treatment time window is likely broader than previously expected for numerous deficits.

Unexpectedly, we observed that a relatively rapid reversal of *Cdkl5* expression led to significant lethality in rescue mice, in line with previous findings from a *Mecp2* reexpression study (34). As with MeCP2, a gradual restoration of CDKL5 expression alleviated this lethality issue and resulted in significant phenotypic reversal. Thus, the time course and dosage of CDKL5 reintroduction need to be carefully considered in future gene-replacement trials to avoid contravening outcomes, particularly in a system that may have partially compensated for its loss (23). Upon completion of tamoxifen delivery and *Cdkl5* reexpression at P60, we waited a substantial amount of time (2 months) prior to evaluating rescue. It remains outstanding to delineate (a) the critical time windows imperative for behavioral rescue; (b) whether distinct time windows exist for different behavioral domains; (c) the temporal nature of the emergence of phenotypic rescue, and (d) the extent of rescue across additional models of CDD, particularly in heterozygous females.

Along this line, we acknowledge that our findings are limited to studies in male mice. In contrast to the pervasive epilepsy in CDD patients, the absence of an overt seizure phenotype in *Cdkl5* mutant male mice could contribute to the success of phenotypic reversibility found in this study. Recently, we uncovered the presence of epileptic spasms and seizure-like behaviors in aged, heterozygous female mouse models of CDD, but not hemizygous *Cdkl5* knockout males or homozygous *Cdkl5* knockout females (43, 44). As we expand our work into modeling the reversibility of CDD-related phenotypes in the relevant heterozygous female population, it will be interesting to establish whether this seizure phenotype alters the extent of rescue with *Cdkl5* restoration, particularly at later time points, and whether a critical time window for treatment exists. This study in hemizygous males highlights the rescue potential across various neurocognitive and motor domains affected by *Cdkl5* loss outside of the influence of epilepsy. However, it remains imperative to extend these experiments to heterozygous females, determine the minimum number of CDKL5-expressing cells needed for phenotypic reversal, and define the latest time window allowable for rescue, at least in mouse models.

CDKL5 is essential for maintaining proper synaptic signaling. The direct impact of CDKL5 loss on pyramidal neuron morphology has been contentious, likely due to context-dependent variability and confounds of mixing cell- and non–cell-autonomous cellular effects. We found that both constitutive and sparse postdevelopmental deletion of CDKL5 increased filipodia-like structures, suggestive of a shift in spine state that, when combined with the absence of changes in overall spine density, reflects a greater proportion of filipodia-like spines on hippocampal CA1 pyramidal neurons (31).

These findings are in line with the observation that CDKL5 is responsible for the phosphorylation of EB2, a member of the microtubule end-binding protein family. End-binding proteins are plus-end–tracking proteins that accumulate at the growing microtubule end and play pivotal roles in microtubule dynamics that mediate cellular architecture, cargo trafficking, and spine stability (45, 46). Thus, CDKL5 may play a role in regulating microtubule dynamics, particularly those related to spine morphology and receptor trafficking at the PSD, via its regulation of microtubule-associated proteins such as EB2. An EB2-related family member, EB3, has previously been implicated in regulating dendritic spine morphology within hippocampal neurons (47). However, the extent to which CDKL5-mediated phosphorylation of EB2 may play similar roles remains undetermined. Interestingly, it has been reported that EB2 suppresses neurite outgrowth and attenuates the microtubule growth mediated by EB1 activity, but how phosphorylation of EB2 at Ser222 specifically modulates this action is untested (48).

We also demonstrate that CDKL5 plays a critical role in maintaining the postsynaptic composition of NMDAR subunits, namely GluN2B. During development, the canonical switch from predominantly GluN2B-containing to predominantly GluN2A-containing NMDARs across the CNS is thought to be a regulatory mechanism involved in shaping circuits and constraining synaptic plasticity during the critical period of synaptogenesis for several brain regions (49). Interestingly, the peak expression of CDKL5 in mouse forebrain appears to coincide with this subunit composition switch during a time window also associated with circuit refinement and acquisition of learning abilities. Loss of CDKL5 may therefore result in an elongated or unconstrained critical period that ultimately leads to maladaptive plasticity across multiple neural circuits and the subsequent heterogeneous collection of symptoms associated with CDD (5). Surprisingly, postdevelopmental restoration of CDKL5 expression reverses the elevation of GluN2B expression and NMDA hyperexcitability phenotype observed in germline knockout mice, arguing that CDKL5 may persistently regulate NMDAR composition beyond the early stages of development. Interestingly, CDKL5 has been reported to target EB2 pS222 via an NMDAR-dependent mechanism, providing a potential link among disrupted NMDAR signaling, microtubule dynamics, and CDKL5 loss-of-function phenotypes (17). Nonetheless, the causal relationship among the molecular, cellular, and behavioral domains examined in this study requires further examination.

Through genetic manipulation of endogenous *Cdkl5* expression in a temporal manner, we show that CDKL5 is required to maintain proper spine morphology, sensory-information processing, and behavioral output in the adult brain. Consistent with this, postdevelopmental restoration of *Cdkl5* expression is sufficient to ameliorate NMDAR-related synaptic deficits and leads to successful reversal of multiple behavioral domains related to CDD. Together, our findings highlight the promise of disease reversal in CDD across a broader-than-expected time window and present an exciting and pressing development for therapeutic treatment of CDD.

Methods

Mice. Mice were group housed in cages of 2 to 5 on a 12-hour light/12-hour dark cycle with food and water provided ad libitum.

Mouse strains and genotyping. The *Cdkl5* conditional (*Cdkl5*^{fl}) and R59X knockin (*Cdkl5*^{R59X}) lines were previously described and are available from the Jackson Laboratory (*Cdkl5*^{fl}: stock no. 030523; R59X: stock no. 028856; refs. 13, 21). UBC-CreER (stock no. 007001), Thy1-GFP line M (Thy1-GFPm; stock no. 007788), and SLICK (stock no. 007610) mice were obtained from the Jackson Laboratory. All lines were maintained in the C57BL/6J background.

Cdkl5^{STOP} mice were generated using the CRISPR-mediated genomic editing technique. A selected gRNA (TGCAACTACAGCATTAGCTCTGG) was chosen upon screening of 12 candidates for targeting specificity and efficacy at intron 3 of the *Cdkl5* locus. The DNA-repairing template constituted a *loxP*-flanked transcriptional STOP cassette, flanked by 817 bp of DNA as the 5′ homologous arm and 1453 bp of DNA as the 3′ homologous arm. Synthesized gRNA and the purified and linearized DNA-repairing template as well as Cas9 mRNA were coinjected into a 1-cell zygote of C57BL/6 background to allow for homology-directed repair, followed by implantation. PCR primers specific to the 5′ and 3′ integration sites flanking the gRNA sequence at *Cdkl5* intron 3 were used to screen for positively targeted pups. Finally, Southern blotting was conducted to confirm the correct targeting of the F1 generation, followed by establishment of a STOP colony in a C57BL/6J genetic background.

Experimental cohorts were all weaned at approximately 3 weeks of age and littermates housed together. *Cdkl5*^{fl}, *Cdkl5*^{R59X}, and Thy1-GFPm mice were genotyped using previously reported PCR-based strategy or with quantitative PCR (qPCR) (Transnetyx Inc.). UBC-CreER and SLICK transgenics were genotyped identically to the Jackson Laboratory strategy. *Cdkl5*^{STOP} mice were genotyped using a qPCR-based strategy optimized by Transnetyx to detect the presence of a *loxP*-flanked STOP cassette within intron 3 of the endogenous *Cdkl5* gene.

Tamoxifen preparation and administration. Tamoxifen (MilliporeSigma, T5648) was dissolved in corn oil (MilliporeSigma, C8267) at a concentration of 20 mg/ml by vortexing and slowly heating the solution at 40°C for 1 hour. Freshly prepared tamoxifen was protected from light by aluminum foil and stored at 4°C for a maximum of 1 week. Animal feeding needles from the Roboz Surgical Store (20 gauge, 1.5 inch length, curved; FN-7910) were used for oral gavage delivery of 0.3 mg/kg of tamoxifen every other day for a total of 5 doses. For adult restoration of *Cdkl5*, a slower dosage timeline originally adapted from Guy et al. was introduced to avoid the lethality associated with rapid reintroduction of CDKL5: 0.3 mg/kg of tamoxifen once a week for a total of 3 weeks and then 2 subsequent deliveries every other day after the third dose (total of 5 doses) (34). See schematics in Figure 1B and Figure 3A for details. All genotypes received tamoxifen within each experimental cohort (except when otherwise noted) to avoid potential confounds introduced by tamoxifen on behaviors (50).

Behavioral assessments. All animal behavioral studies were carried out blinded to genotype. Mice were habituated to the testing room for at least 1 hour before testing (except for context- and cue-dependent fear-conditioning assays), which was always performed at the same time of day. Testing was performed in the same order for each animal, beginning with the elevated zero maze assay, then the open-field test, Y maze, 3-chambered social-approach assay, accelerating rotarod assay, context- and cue-dependent fear conditioning, repetitive behavior assay, olfaction, and hind limb clasping, as previously described (13, 21). Behavioral data were analyzed by researchers blinded to genotype. See Supplemental Methods for details on all behavioral assays.

ERPs. ERP surgeries, recordings, and analyses were performed as previously described in Wang et al. and Goffin et al. (9, 51). Mice underwent stereotaxic implantation with a stainless-steel recording electrode placed at 2.0 mm posterior, 2.0 mm left lateral relative to bregma, and –1.8 mm depth. Ground and reference electrodes were placed posterior of the hippocampal electrode at 1.0 mm and 2.0 mm distances, respectively. EEG recordings were performed on freely mobile, nonanesthetized mice in their home cage environment after a 20-minute acclimation to the recording room. Recordings were performed using Spike2 software connected to a Power 1401 II interface module (CED) and high-impedance differential AC amplifier systems (A-M Systems). Signals were acquired at 1667 Hz and band-pass filtered between 1 and 500 Hz with a 60 Hz notch filter and gain of 1000. ERPs were recorded by presentation of auditory stimuli consisting of 250 repeats of white noise (85 dB sound pressure, 10 ms duration) at 4-second interrepeat intervals. ERP traces were generated by averaging across single-trial epochs centered at $t = 0 \pm 2$ seconds. Single trials were baseline corrected by subtracting the temporal mean at $t = -1$ seconds to $t = 0.5$ seconds. Altering the baseline closer to sound presentation had no effect on the results shown. The mean ERP amplitudes were subsequently calculated across 250 trials. Event-related power and phase were computed as functions of frequency and time, as previously described (51).

Brain microdissection. Brains were removed and sectioned into 1 mm coronal slices using a mouse brain matrix. Tissue was dissected from regions of interest and homogenized in RIPA lysis buffer (150 mM NaCl, 1% Triton X-100, 0.5% sodium deoxycholate, 0.1% sodium dodecyl sulfate, 25 mM Tris [pH7.4] with protease inhibitors [Roche, cOmplete, EDTA-free Protease Inhibitor Cocktail Tablets; 5056489001]). To prepare protein extracts, homogenized lysates were incubated on ice for 15 minutes and then centrifuged at 21,000 *g* for 15 minutes at 4°C. The supernatant fraction was removed and sonicated using a Biorupter (Diagenode) for 3 alternating sessions at a maximum frequency for 15 seconds, each followed by a 60-second cooldown period. The lysate was then centrifuged at 21,000 *g* for 15 minutes at 4°C and the top aqueous layer carefully removed and collected as the total protein fraction.

PSD protein purification. We adapted a previous protocol for the preparation of postsynaptic density (PSD) fractions (13, 52). Forebrain cortical tissues were microdissected and Dounce-homogenized in 10 mL of homogenization buffer (0.32 M sucrose, 4 mM HEPES, pH 7.4 with protease inhibitors [Roche, cOmplete, EDTA-Free Protease Inhibitor Cocktail Tablets; 5056489001]). The homogenate was centrifuged at 1000 *g* for 10 minutes at 4°C to pellet cellular debris and nuclei (P1), and the subsequent supernatant (S1) was centrifuged for another 15 minutes at 10,000 *g* at 4°C. The resulting pellet (P2, "crude" synaptosomes) was resuspended in another 10 mL of homogenization buffer and centrifuged at 10,000 *g* for 15 minutes at 4°C. The supernatant was discarded, and the resulting pellet (P2′) was resuspended in 10 mL of 4 mM HEPES (pH 7.4), then homogenized on ice. The lysate was incubated at 4°C for 30 minutes while shaking to hypoosmotically lyse the synaptosomes and then centrifuged for 20 minutes at 25,000 *g* at 4°C. The resultant pellet (LP1) was resuspended in 1 mL of homogenization buffer and layered on top of a discontinuous sucrose gradient (bottom to top: 1.5 mL of 1.2M sucrose, 1 mL of 1.0M sucrose, and 1 mL of 0.8M sucrose). The gradient was ultracentrifuged at 150,000 *g* for 1.5 hours at 4 °C. The turbid layer between the 1.0M/1.2M sucrose interphase containing the synaptic plasma membranes (~1 mL) was collected and resuspended in 5 mL of 4 mM HEPES to dilute out the sucrose. This fraction was ultracentrifuged again at 200,000 *g* for 30 minutes at 4°C. The resulting pellet was resuspended in 1 mL of 50 mM HEPES with 2 mM EDTA (pH 7.4) and the membrane proteins extracted by adding Triton X-100 at a final concentration of 0.5% and incubating at 4°C while rotating for 15 minutes. The proteins were centrifuged at 32,000 *g* for 20 minutes at 4°C and the resulting pellet resuspended in 75 μL of 50 mM HEPES with 2 mM EDTA.

Western blot. Protein concentration was measured using a Bradford assay. Either 7.5 μg or 25 μg of protein was loaded into each well of a 4% to 12% Bis-Tris gradient gel (Invitrogen, 10 well, 1.5 mm; NP0335) for PSD protein or brain lysate, respectively. Protein gels were run for 2 hours at 125 V (3 hours at 100V for Western blots in Supplemental Figures 6 and 7 to allow for specific examination of crossreacting bands at the position of full-length CDKL5 protein), then transferred onto a PVDF membrane (0.45 μm pore size; Bio-Rad, 162–0115). The resulting membrane was blocked with a 1:1 solution of Odyssey blocking buffer (LICOR; 927-40100) and 1× PBS for 1 hour at room temperature.

Primary antibodies used were rabbit anti–N-terminal CDKL5 (in house, previously described, ref. 9; 1:500), anti–C-terminal CDKL5 (Millipore, catalog ABS402; 1:250), anti-CDKL5 (MRC Dundee, catalog SA145; 1:1000), mouse anti–β-actin (Abcam; catalog ab8226; 1:10,000), rat anti-EB2(K52) (Abcam, catalog ab45767; 1:10,000), and rabbit anti–phospho-EB2(S222) (provided by Sila Ultanir, Francis Crick Institute, London, United Kingdom; 1:1000). For PSD studies, the primary antibodies used were rabbit anti–N-terminal CDKL5 (as above), mouse anti-GluN1 (Thermo Fisher, catalog OMA1–04010; 1:1000), rabbit anti-GluN2A (Frontier Institute, catalog AB_2571605; 1:200), rabbit anti-GluN2B (Frontier Institute, catalog AB_2571761; 1:200), rabbit anti-GluA1 (Abcam, catalog ab31232; 1:5000), rabbit anti-GluA2 (Abcam, catalog ab133477; 1:5000), and anti-β-actin (as above). Secondary antibodies (LI-COR) used were goat anti-rabbit IgG (IRDye 800CW, catalog 926-32211), goat anti-mouse IgG (IRDye 680LT, catalog 926-68020), and goat anti-rat IgG (IRDye 680LT, catalog 926-68029), all incubated for 50 minutes at room temperature at dilutions of 1:10,000. Standard protocols were used for the Odyssey Infrared Imaging System (LI-COR) for protein visualization and quantification.

Dendritic spine analysis. All steps of sectioning, imaging, and data analysis were performed by a researcher blinded to genotype. Adult male mice at P120 were transcardially perfused with 4% paraformaldehyde and their brains subsequently extracted and postfixed additionally overnight at 4°C. Brains were cryoprotected upon overnight fixation by infiltration in 15% sucrose and subsequently 30% sucrose in PBS and then frozen in OCT (Sakura Finetek). Frozen brains were sectioned coronally at 50 μm on a Leica CM3050S cryostat. For spine imaging, unstained sections were mounted with ProLong Glass Antifade Mountant (Thermo Fisher; P36982).

GFP-positive pyramidal neurons located in the hippocampal CA1 region (approximately between bregma coordinates –1.34 to –1.94) with well-preserved morphology were chosen for imaging. For dendritic spines, secondary and tertiary dendritic branches of basal and proximal apical dendrites, excluding the apical tuft, of CA1 pyramidal neurons were imaged. Image stacks were taken with a 63×/1.40 NA oil-immersion objective at 4× zoom. Each dendritic segment was centered in a field of view with dimensions 43.93 × 10.95 μm, with a step size of 0.22 μm and total depth spanning less than 7 μm.

All image analysis was performed by a researcher blinded to genotype. For spine analysis, 3D blind deconvolution was first performed on confocal image stacks with an iterative constrained Tikhonov-Miller algorithm (DeconvolutionLab, ImageJ, NIH) using a pointspread function generated from the imaging parameters (PSF Generator, ImageJ). The deconvolved image stack was imported into Imaris and analyzed. The dendritic backbone of each segment was first traced using the autopath function, and a cone-type dendrite diameter was built using a contrast threshold of 0.2 and dendrite maximum diameter of 1 μm. Spines were manually traced on each dendrite using the autopath function, with a cutoff of a maximum distance of 3 μm from the dendritic backbone. Automated spine reconstruction of manually traced spines was performed using the Imaris Bitplane Wizard builder. Imaris was used to perform automated computation of spine density and estimation of morphometric parameters for individual spines, including spine length, terminal point (head) diameter, and volume. Note that the YFP signal produced by the SLICK line provided suboptimal fluorescent signal for dendritic spine head measurement, resulting in reduced spine head diameter and volume metrics compared with what was expected and previously reported.

NMDA-induced seizure scoring. Seizures were induced in P180 mice by intraperitoneal administration of 90 mg/kg NMDA (Sigma-Aldrich; M3262) in sterile 0.9% PBS. Seizure progression was scored using a modified Racine scale as previously described: 0, no abnormality; 1, exploring, sniffing, and grooming ceased, animal becomes motionless; 2, forelimb and/or tail extension, appearance of rigid posture; 3, myoclonic jerks of the head and neck, with brief twitching movement, or repetitive movements with head bobbing or "wet-dog shakes"; 4, forelimb clonus and partial rearing, or rearing and falling; 5, forelimb clonus, continuous rearing and falling; 6, tonic-clonic movements with loss of posture tone, often resulting in death (35). After drug injection, maximum seizure scores were recorded within a 30-minute observation period.

Electrophysiology recordings. Mice were deeply anesthetized using isoflurane and perfused transcardially with ice-cold ACSF (pH 7.3–7.4) containing the following: 124 mM NaCl, 2.5 mM KCl, 1.2 mM NaH_2PO_4, 24 mM $NaHCO_3$, 5 mM HEPES, 12.5 mM glucose, 1.3 mM $MgSO_4$, 7 mM H_2O, 2.5 mM $CaCl_2$. The brain was rapidly removed, and transverse sections (400 μM) were cut on a vibratome (VT 1200s, Leica). Slices were incubated in a holding chamber for 12 to 15 minutes at 32 to 34°C in a NMDG-based recovery solution (pH 7.3–7.4, pH adjusted with HCl): 92 mM NMDG, 2.5 mM KCl, 1.2 mM NaH_2PO_4, 30 mM $NaHCO_3$, 20 mM HEPES, 25 mM glucose, 5 mM sodium ascorbate, 2 mM thiourea, 3 mM sodium pyruvate, 10 mM $MgSO_4$, 7 mM H_2O, 0.5 mM $CaCl_2$. Osmolarity for the NMDG-based solution and ACSF was kept between 300 and 310 mOsm. Following incubation, slices were moved to a second holding chamber containing ACSF at room temperature (20–22°C) for at least 1 hour prior to recording. For recording, slices were transferred to the recording chamber (Scientifica) fully submerged in oxygenated (95% O_2, 5% CO_2) ACSF at a perfusion rate of 1.4 to 1.6 mL/min, bath temperature of 29 to 30°C, and secured using a slice anchor (Warner Instruments). Electrophysiology data were acquired using custom-built Recording Artist software version (managed by Rick Gerkin) Igor Pro 6.37 (Wavemetrics). All recordings were sampled at 20 k Hz and filtered at 2.8 kHz.

Evoked AMPA/NMDA currents. CA1 pyramidal neurons were visualized using differential interference contrast (DIC) video microscopy on an upright microscope (Olympus, BX51). Somatic whole-cell recordings were performed using borosilicate glass (World Precision Instruments, TW150-3) that had a tip resistance of 3 to 5 MΩ, filled with cesium-based internal solution for voltage-clamp recordings: 115 mM $CsMeSO_3$, 20 mM CsCl, 10 mM HEPES, 0.6 mM EGTA, 2.5 mM MgCl, 10 mM Na-phosphocreatine, 4 mM Na-ATP, 4 mM Na-GTP, 0.1 mM Spermine, 1 QX-314 (pH adjusted to 7.3–7.4 with CsOH). A bipolar θ glass electrode backfilled with ACSF was positioned in the Schaffer collaterals for electrical stimulation. Stimulation intensity was adjusted to evoke single-component EPSCs with a frequency of 0.1 Hz. Voltage-clamp traces were recorded at a holding potential of –70 mV (for AMPA-EPSCs) or +40 mV (for NMDA-EPSCs) in the presence of 100 μM picrotoxin (Sigma-Aldrich). For each cell, at least 15 traces were averaged to obtain a representative response at each holding potential. The peak EPSC amplitude at –70 mV was taken as the magnitude of the AMPA-EPSCs. To isolate the NMDA-mediated current, 10 μM NBQX (Abcam) was bath applied and the blockade of AMPA-mediated currents was confirmed at –70mV. To calculate the NMDA/AMPA ratio, the amplitude taken at +40 mV in the presence of NBQX was divided by the peak amplitude of the AMPA-EPSC at –70 mV. The access resistance was monitored throughout the experiment, and data were excluded if access resistance increased above 20 MΩ. The decay time constant of NMDAR-mediated EPSCs was calculated with a single-exponential fit in Igor 7.

Statistics. For behavioral assays, we chose similar sample sizes for all behavioral experiments based on previous published studies of CDD mouse models (9, 13, 21). The number of mice used was predetermined prior to the start of each experiment. All data sets were analyzed using the Shapiro-Wilk test for normality. For 1-sample comparisons, data sets with normal distributions were analyzed for significance using the 1-sample *t* test, whereas data sets with nonnormal distributions were analyzed using Wilcoxon's signed-rank test. For 2-sample comparisons, data sets with normal distributions were analyzed for significance using the unpaired Student's *t* test, whereas data sets with nonnormal distributions were analyzed using the Mann-Whitney *U* test. Two-way repeated measures ANOVA or the Kruskal-Wallis test was conducted for the appropriate data sets with post hoc Holm-Šidák's or Dunn's multiple-comparison tests. All 1-sample, 2-sample, and multiple-comparison tests were 2-tailed.

For NMDA seizure induction, we tested a pilot cohort of WT and *Cdkl5* knockout animals at various doses of NMDA to establish an effect size in our own hands on this reported phenotype. This enabled proper power analysis to determine the appropriate sample size (Supplemental Figure 10 at 90 mg/kg). Maximum seizure scores were statistically analyzed using the Kruskal-Wallis test and post hoc Dunn's multiple-comparison test for significance. Similarly, we referenced reported effect sizes for NMDA/AMPA ratio phenotypes from previous studies in order to determine proper sample sizes for our physiology experiments. To analyze significance, we conducted 1-way ANOVA with post hoc Tukey's multiple-comparison test.

All other assays that involved subsampling of animals were analyzed using R (The R Project for Statistical Computing), as previously described (13). Each data set was analyzed using a linear mixed effect model, where *genotype* was modeled as a fixed effect term and *animal* was modeled as a random effect term. This model accounts for both between-animal and between-cell variations. For each assay, null and alternative models were constructed using the *lmer* function in the lme4 package in the following format: m0 = lmer(outcome ~ (1|animal), REML = TRUE); m1 = lmer(outcome ~ genotype + (1|animal), REML = TRUE). To make statistical comparisons, the *KRmodcomp* function from the pbkrtest package (53) was used:KRmodcomp(m0, m1). The KRmodcomp function reports a modified *F* test statistic based on the Kenward and Roger approximation and accounts for the small sample sizes in our study, modified numerator and denominator degrees of freedom, and a *P* value. The estimated effect of *genotype* is obtained from the alternative model constructed using the *lmer* function from lme4.

All graphs are plotted using Prism (GraphPad). Bolded center lines reflect the mean, and all error bars indicate SEM. For box plots, the limits indicate the minimum and maximum, with the box plot center line indicating the median.

Study approval. Experiments were conducted in accordance with the ethical guidelines of the NIH and with the approval of the Institutional Animal Care and Use Committee of the University of Pennsylvania.

Author contributions

BT and ZZ designed the experiments and reviewed and interpreted the data. BT, MFD, YH, and ST performed the experiments with assistance from YTL and ZX. YC managed all mouse colonies. MVF provided valuable experimental feedback and guidance. BT and ZZ wrote the manuscript with input from all other authors.

Acknowledgments

This work was supported by funding from The Loulou Foundation (to ZZ), the International Foundation for CDKL5 Research (to ZZ), the Intellectual and Developmental Disabilities Research Center (IDDRC) at CHOP/PENN U54HD086984 (to ZZ and MVF), R01NS102731 (to ZZ), F31NS101762 (to BT), and F30NS100433 (to ST). MFD is a Howard Hughes Medical Institute Gilliam Fellow. The authors would like to thank Sila Ultanir at the Francis Crick Institute (London, United Kingdom) for generously sharing antibodies against phosphorylation of EB2, as well as Erin Nugent, Bing Xu, Xie Song, and Joshua Ross from the Zhou laboratory for their assistance in assessing behavioral phenotypes.

Address correspondence to: Zhaolan Zhou, Clinical Research Building Room 460, 415 Curie Boulevard, Philadelphia, Pennsylvania 19104, USA. Phone: 215.746.5025; Email: zhaolan@pennmedicine.upenn.edu.

---

1. Kalscheuer VM, et al. Disruption of the serine/threonine kinase 9 gene causes severe X-linked infantile spasms and mental retardation. *Am J Hum Genet*. 2003;72(6):1401–1411.
2. Tao J, et al. Mutations in the X-linked cyclin-dependent kinase-like 5 (CDKL5/STK9) gene are associated with severe neurodevelopmental retardation. *Am J Hum Genet*. 2004;75(6):1149–1154.
3. Weaving LS, et al. Mutations of CDKL5 cause a severe neurodevelopmental disorder with infantile spasms and mental retardation. *Am J Hum*

Genet. 2004;75(6):1079–1093.

4. Fehr S, et al. The CDKL5 disorder is an independent clinical entity associated with early-onset encephalopathy. *Eur J Hum Genet*. 2013;21(3):266–273.
5. Olson HE, et al. Cyclin-dependent kinase-like 5 deficiency disorder: clinical review. *Pediatr Neurol*. 2019;97:18–25.
6. Demarest ST, et al. CDKL5 deficiency disorder: Relationship between genotype, epilepsy, cortical visual impairment, and development. *Epilepsia*. 2019;60(8):1733–1742.
7. Liang JS, et al. Phenotypic manifestations between male and female children with CDKL5 mutations. *Brain Dev*. 2019;41(9):783–789.
8. Symonds JD, et al. Incidence and phenotypes of childhood-onset genetic epilepsies: a prospective population-based national cohort. *Brain*. 2019;142(8):2303–2318.
9. Wang IT, et al. Loss of CDKL5 disrupts kinome profile and event-related potentials leading to autistic-like phenotypes in mice. *Proc Natl Acad Sci U S A*. 2012;109(52):21516–21521.
10. Archer HL, et al. CDKL5 mutations cause infantile spasms, early onset seizures, and severe mental retardation in female patients. *J Med Genet*. 2006;43(9):729–734.
11. Amendola E, et al. Mapping pathological phenotypes in a mouse model of CDKL5 disorder. *PLoS One*. 2014;9(5):e91613.
12. Okuda K, et al. Comprehensive behavioral analysis of the Cdkl5 knockout mice revealed significant enhancement in anxiety- and fear-related behaviors and impairment in both acquisition and long-term retention of spatial reference memory. *PLoS One*. 2018;13(4):e0196587.
13. Tang S, et al. Altered NMDAR signaling underlies autistic-like features in mouse models of CDKL5 deficiency disorder. *Nat Commun*. 2019;10(1):2655.
14. Kilstrup-Nielsen C, et al. What we know and would like to know about CDKL5 and its involvement in epileptic encephalopathy. *Neural Plast*. 2012;2012:728267.
15. Ricciardi S, et al. CDKL5 ensures excitatory synapse stability by reinforcing NGL-1-PSD95 interaction in the postsynaptic compartment and is impaired in patient iPSC-derived neurons. *Nat Cell Biol*. 2012;14(9):911–923.
16. Zhu YC, et al. Palmitoylation-dependent CDKL5-PSD-95 interaction regulates synaptic targeting of CDKL5 and dendritic spine development. *Proc Natl Acad Sci U S A*. 2013;110(22):9118–9123.
17. Baltussen LL, et al. Chemical genetic identification of CDKL5 substrates reveals its role in neuronal microtubule dynamics. *EMBO J*. 2018;37(24):e99763.
18. Muñoz IM, et al. Phosphoproteomic screening identifies physiological substrates of the CDKL 5 kinase. *EMBO J*. 2018;37(24):e99559.
19. Della Sala G, et al. Dendritic spine instability in a mouse model of CDKL5 disorder is rescued by insulin-like growth factor 1. *Biol Psychiatry*. 2016;80(4):302–311.
20. Lupori L, et al. Site-specific abnormalities in the visual system of a mouse model of CDKL5 deficiency disorder. *Hum Mol Genet*. 2019;28(17):2851–2861.
21. Tang S, et al. Loss of CDKL5 in glutamatergic neurons disrupts hippocampal microcircuitry and leads to memory impairment in mice. *J Neurosci*. 2017;37(31):7420–7437.
22. Zhu YC, Xiong ZQ. Molecular and synaptic bases of CDKL5 disorder. *Dev Neurobiol*. 2019;79(1):8–19.
23. Benke TA, Kind PC. Proof-of-concept for a gene replacement approch to CDKL5 deficiency disorder. *Brain*. 2020;143(3):716–718.
24. Ruzankina Y, et al. Deletion of the developmentally essential gene ATR in adult mice leads to age-related phenotypes and stem cell loss. *Cell Stem Cell*. 2007;1(1):113–126.
25. Hensch TK. Critical period regulation. *Annu Rev Neurosci*. 2004;27(1):549–579.
26. McGraw CM, et al. Adult neural function requires MeCP2. *Science*. 2011;333(6039):186.
27. Kiermayer C, et al. Optimization of spatiotemporal gene inactivation in mouse heart by oral application of tamoxifen citrate. *Genesis*. 2007;45(1):11–16.
28. Saby JN, et al. Evoked potentials and EEG analysis in rett syndrome and related developmental encephalopathies: towards a biomarker for translational research. *Front Integr Neurosci*. 2020;14:30.
29. Wijetunge LS, et al. Stimulated emission depletion (STED) microscopy reveals nanoscale defects in the developmental trajectory of dendritic spine morphogenesis in a mouse model of fragile X syndrome. *J Neurosci*. 2015;34(18):6405–6412.
30. Feng G, et al. Imaging neuronal subsets in transgenic mice expressing multiple spectral variants of GFP. *Neuron*. 2000;28(1):41–51.
31. Harris KM, Stevens JK. Dendritic spines of CA1 pyramidal cells in the rat hippocampus: serial electron microscopy with reference to their biophysical characteristics. *J Neurosci*. 1989;9(8):2982–2997.
32. Young P, et al. Single-neuron labeling with inducible Cre-mediated knockout in transgenic mice. *Nat Neurosci*. 2008;11(6):721–728.
33. Szafranski P, et al. Neurodevelopmental and neurobehavioral characteristics in males and females with CDKL5 duplications. *Eur J Hum Genet*. 2015;23(7):915–921.
34. Guy J, et al. Reversal of neurological defects in a mouse model of Rett syndrome. *Science*. 2007;315(5815):1143–1147.
35. Okuda K, et al. CDKL5 controls postsynaptic localization of GluN2B-containing NMDA receptors in the hippocampus and regulates seizure susceptibility. *Neurobiol Dis*. 2017;106:158–170.
36. Angelakos CC, Abel T. Molecular genetic strategies in the study of corticohippocampal circuits. *Cold Spring Harb Perspect Biol*. 2015;7(7):a021725.
37. Gao Y, et al. Gene replacement ameliorates deficits in mouse and human models of cyclin-dependent kinase-like 5 disorder. *Brain*. 2020;143(3):811–832.
38. Fuccillo MV. Striatal circuits as a common node for autism pathophysiology. *Front Neurosci*. 2016;10:27.
39. Mei Y, et al. Adult restoration of Shank3 expression rescues selective autistic-like phenotypes. *Nature*. 2016;530(7591):481–484.
40. Creson TK, et al. Re-expression of SynGAP protein in adulthood improves translatable measures of brain function and behavior. *Elife*. 2019;8:e46752.
41. Ozonoff S, et al. The onset of autism: patterns of symptom emergence in the first years of life. *Autism Res*. 2008;1(6):320–328.
42. Zoghbi HY, Bear MF. Synaptic dysfunction in neurodevelopmental disorders associated with autism and intellectual disabilities. *Cold Spring Harb Perspect Biol*. 2012;4(3):a009886.
43. Terzic B, et al. X-linked cellular mosaicism underlies age-dependent occurrence of seizure-like events in mouse models of CDKL5 deficiency disorder. *Neurobiol Dis*. 2021;148:105176.
44. Mulcahey PJ, et al. Aged heterozygous Cdkl5 mutant mice exhibit spontaneous epileptic spasms. *Exp Neurol*. 2020;332:113388.
45. Komarova Y, et al. Mammalian end binding proteins control persistent microtubule growth. *J Cell Biol*. 2009;184(5):691–706.
46. Akhmanova A, Steinmetz MO. Control of microtubule organization and dynamics: two ends in the limelight. *Nat Rev Mol Cell Biol*. 2015;16(12):711–726.
47. Leterrier C, et al. End-binding proteins EB3 and EB1 link microtubules to ankyrin G in the axon initial segment. *Proc Natl Acad Sci U S A*. 2011;108(21):8826–8831.
48. Laketa V, et al. High-content microscopy identifies new neurite outgrowth regulators. *Mol Biol Cell*. 2006;18(1):242–252.
49. Paoletti P, et al. NMDA receptor subunit diversity: impact on receptor properties, synaptic plasticity and disease. *Nat Rev Neurosci*. 2013;14(6):383–400.
50. Liu Z, et al. Short-term tamoxifen treatment has long-term effects on metabolism in high-fat diet-fed mice with involvement of Nmnat2 in POMC neurons. *FEBS Lett*. 2018;592(19):3305–3316.
51. Goffin D, et al. Rett syndrome mutation MeCP2 T158A disrupts DNA binding, protein stability and ERP responses. *Nat Neurosci*. 2012;15(2):274–283.
52. Bermejo MK, et al. Preparation of synaptic plasma membrane and postsynaptic density proteins using a discontinuous sucrose gradient. *J Vis Exp*. 2014;(91):e51896.
53. Halekoh U, Højsgaard S. A Kenward-Roger approximation and parametric bootstrap methods for tests in linear mixed models –the R package pbkrtest. *J Stat Softw*. 2014;59(9):1–32.